Chapter 8
Solar Tracking Error in Solar-Pumped Lasers

Bruno D. Tibúrcio

8.1 Brief Introduction

In this chapter are discussed the solar tracking errors and the compensation techniques in solar-pumped lasers. Solar tracking error displaces the focal spot away from its optimal position, shifting the center of the absorption distribution within the laser rod, resulting in less laser output power and poor laser beam quality. The multi-rod approach is here discussed numerically and experimentally, in order to compensate the solar tracking error and enhance stable solar laser emission. A numerical modeling example of solar-pumped laser with tracking error compensation capacity is finally given in this chapter.

8.2 Sun Trajectory and Error Formation in Solar Energy Collection and Concentration Systems

8.2.1 Sun Trajectory in the Sky During the Day

The conceptualization of the apparent movement of the Sun is of paramount importance in the development of solar energy systems and solar tracking error systems. The discussion that follows is made within the context of orientating a solar tracker with respect to the Sun at any location on the earth and on any given time of the day. In the Fig. 8.1 below is shown the schematics of the Sun-Earth relationship. As seen from the Earth, the Sun disk forms an angle of 32 min of a degree. The Sun cannot be considered as a point source, due to even this small angle is significant in the analysis of the optical efficiency of a solar concentration system.

Knowledge of the variation in the Sun's position along the time and through the sky is necessary to calculate the solar radiation falling on a surface. The relative motions of the sun and earth are not simple, but they are systematic and thus predictable [1].

D. Liang et al., *Solar-Pumped Lasers*, Green Energy and Technology,
https://doi.org/10.1007/978-3-031-24785-9_8

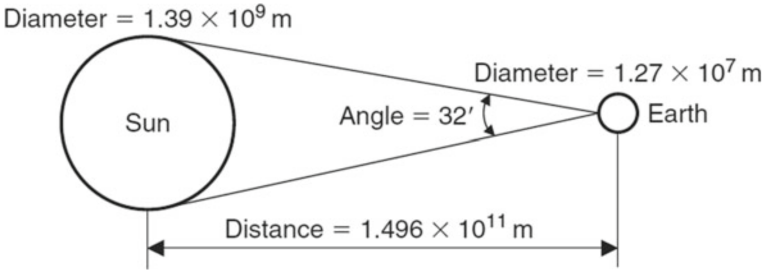

Fig. 8.1 Sun-earth relationship, adapted from [1]

The Ptolemaic view of the Sun's motion is used in the analysis for simplicity; since all motion is relative, it is convenient to consider the Earth fixed and to describe the Sun's apparent motion in a coordinate system fixed to the earth with its origin at the site of interest. Solar tracking systems (STS), such as the altitude-azimuth dual axis, use solar tracking algorithms to ensure that the Sun's passage through the sky is calculated and followed with high precision in automated solar tracker applications. A high precision solar position calculator or algorithm uses a software program routine to align the solar tracker to the sun and is an important component in the design and construction of an automatic solar tracking system. Solar position computer software for tracing the sun is available as open source codes.

The Earth makes one rotation about its axis every 24 h and completes a revolution about the sun in a period of approximately 365.25 days. The eccentricity, e, of the earth's orbit is very small, equal to 0.01673. Therefore, the orbit of the earth around the sun can be approximated as circular. Any location on the surface of the earth then can be defined by the intersection of a longitude angle and a latitude angle [2].

The Sun is constrained to move with 2 degrees of freedom on the celestial sphere; therefore, its position with respect to an observer on earth can be fully described by means of two astronomical angles, the solar altitude (h) and the solar azimuth (α) angles. Before giving the equations of solar altitude and azimuth angles, the solar declination and hour angle need to be defined.

8.2.2 Error Formation in Solar Energy Collection and Concentration Systems

The movement of the earth affects the collected solar radiation on solar systems, and consequently on the efficient solar concentration. The variation of the Sun's position in the sky during the day, or its apparent movement, generates errors in the alignment of the solar energy concentration system and the Sun, which any STS is designed to attenuate with a certain degree of accuracy with its automatic movement. The necessity of a high precision STS become a critical key for the developing and deploying of solar concentration systems with the smallest integrated error in the STS.

Declination, δ

The earth axis of rotation (the polar axis) is always inclined at an angle of 23.45° from the ecliptic axis, which is normal to the ecliptic plane [1]. The ecliptic plane is the plane of orbit of the earth around the sun. The solar declination (δ) is the angle between the line joining the centers of the Sun and the Earth and its projection on the equatorial plane, as shown in Fig. 8.2. Declinations north of the equator (summer in the Northern Hemisphere) are positive, and those south are negative, and is given by:

$$\delta = 23.45 \sin\left[\frac{360}{365}(284 + N)\right] \tag{8.1}$$

The declination, δ, in degrees for any day of the year (N) can be calculated approximately by the equation [1]:

The solar declination during any given day can be considered constant in engineering calculations [4, 5]. The variation of the solar declination throughout the year is shown in Fig. 8.3.

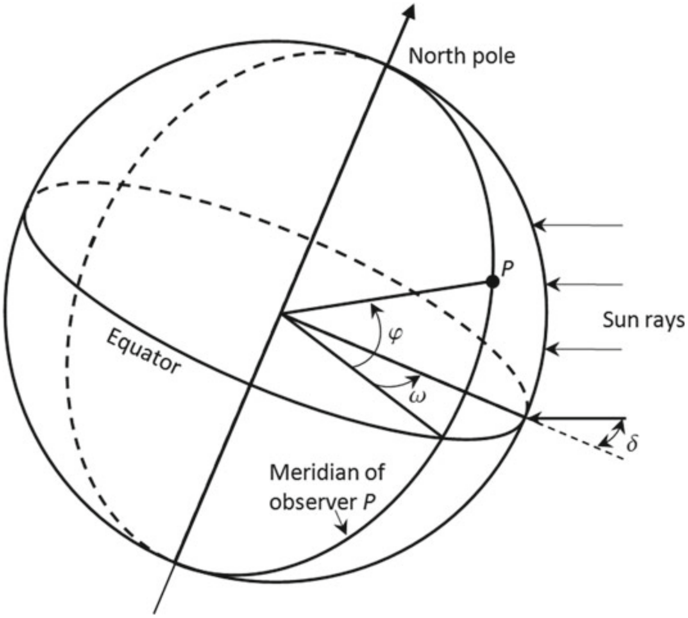

Fig. 8.2 Representative drawing of latitude, solar declination and hour angle, adapted from [3]

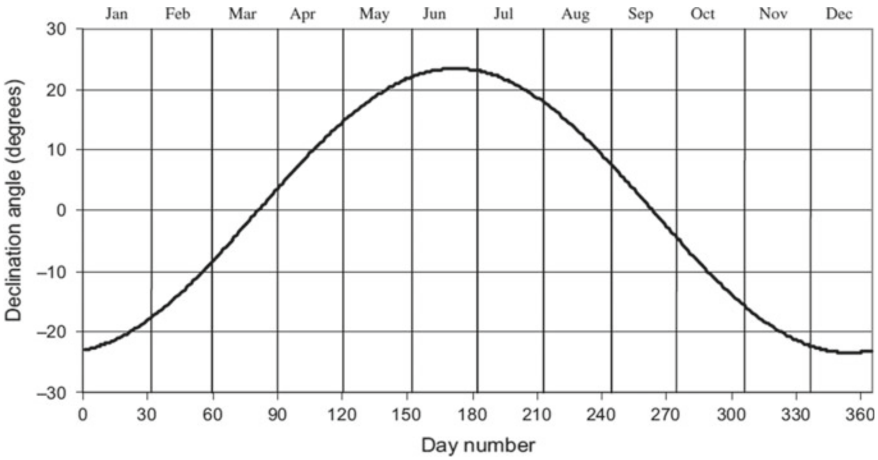

Fig. 8.3 Solar declination angle of the Sun [1]

Hour angle, ω

The hour angle, ω, of a point on the earth's surface is defined as the angle through which the earth would turn to bring the meridian of the point directly under the sun. To describe the Earth's rotation about its polar axis the concept of hour angle (ω) is used, which is the angle between the meridian passing through the Sun and the meridian of the observer P, as shown in Fig. 8.2, and is given by [1]:

$$\omega = \pm 0.25^{\circ} \times number\ of\ minutes\ from\ local\ solar\ noon \tag{8.2}$$

where the plus sign applies to afternoon hours and the minus sign to morning hours. The hour angle at local solar noon is zero, with each 360/24 or 15° of longitude equivalent to 1 h, afternoon hours being designated as positive.

Solar altitude angle, h

The solar rays are characterized by two astronomical angles: solar azimuth angle and the solar altitude angle [1, 6]. The solar altitude angle (h) is defined as the vertical angle between the projection of the Sun's rays on the horizontal plane, as shown in the Fig. 8.4. It is related to the solar zenith angle (θ_Z) which is the angle between the Sun's rays and the vertical [1]:

$$\theta_Z = 90^{\circ} - h \tag{8.3}$$

The solar altitude angle at the time of Sunrise and Sunset is 0°. The solar altitude angle has its maximum value at noon time in all seasons. The elevation angle is related to both the declination angle and the hour angle by the following expression [1].

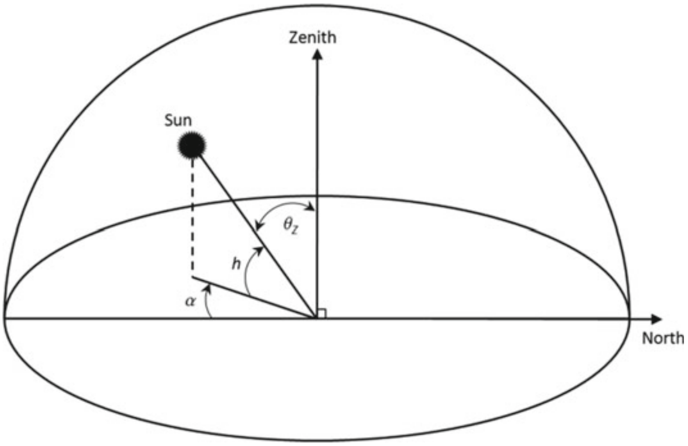

Fig. 8.4 Solar altitude h, azimuth α and zenith angles θ_Z

$$\sin(h) = \cos(\varphi)\cos(\delta)\cos(\omega) + \sin(\varphi)\sin(\delta) \tag{8.4}$$

where φ is the local latitude in degrees. The solar altitude angle at the time of sunrise and sunset is 0°, and has its maximum value at noon time in all seasons.

Solar azimuth angle, α

The solar azimuth angle, α, is the angle of the sun's rays measured in the horizontal plane from due south (true south) for the Northern Hemisphere or due north for the Southern Hemisphere; westward is designated as positive. For a geographical location, the azimuth angle α is the horizontal angle of the Sun's rays, and is given by the following equation [1]:

$$\sin(\alpha) = \frac{\cos(\delta)\sin(\omega)}{\cos(h)} \tag{8.5}$$

The output power produced by high-concentration solar systems is directly related to the amount of solar energy collected by the system, and it is necessary to track the sun's position with a high degree of accuracy, thus decreasing the errors in the alignment of the Sun and the solar concentration system.

8.3 Solar Tracking Systems

8.3.1 Direct Solar Tracking Mode

Solar-pumped lasers have additional problems not seen in commercial lasers in achieving the maximum solar energy transfer and absorption efficiencies from the pump source to the laser medium. The resonator stability of solar lasers depends on how well the Sun is tracked to continuously pump the laser crystal. The output power produced by high-concentration solar thermal and solar laser and photovoltaic systems is directly related to the amount of solar energy collected by the system. Many solar tracking systems (STS) have been proposed to implement this task over the past 60 years. STS thus have an important role in the development and efficiency of solar concentration applications [6]. STS enable solar collectors to accurately point towards the Sun and compensate for time (day and season) changes observed in altitude and azimuth angles of the Sun, thus decreasing the errors formed by the apparent movement of the Sun.

In this chapter, the STS will be presented regarding the fact if the primary collectors continuously follow the Sun directly pointed to it (or are tilted in a determined angle in order to increase its efficiency), or if the collectors are fixed, but irradiated by heliostats continuously moving to track the Sun's apparent movement in the sky.

There are different classifications of tracking systems regarding the strategies implemented to increase the energy collected by solar systems. Passive STS have simple operation principles, without mechanical parts or sensing units to help it to orient towards the Sun [7, 8], however, they have lower accuracy and energy gain compared to their more complex counterparts [9]. Active STS usually have optical sensors that help them to continuously determine the position of the Sun and use the motors to adjust the axes orientation [2]. In relation to the control strategies used to implement STS, there are the closed loop systems and the open-loop systems, the former based on feedback control principles, receiving input signals from the sensors which determine the position of the Sun [10–12]. The latter are algorithm-based systems, without feedback control to correct errors or disturbances in the operation [13–15].

STS can also be classified regarding to the number of movable axis following the Sun. They are generally classified in those implemented by using single-axis STS, and for higher accuracy, double-axis STS. There are several configurations of motion of single-axis trackers: horizontal, tilted-horizontal, vertical, tilted and polar aligned, parallel to earth's axis, with east–west tracking [1, 9]. Studies have demonstrated that single-axis STS [16–20] can increase their energy produced of between 12 and 20% [21] compared with fixed/optimally inclined installations.

Although single-axis trackers are cheaper and easier to build and implement, the increase in efficiency provided is lower than that of the double-axis STS [9]. These systems have been studied using Fresnel lenses [22] or concentrator photovoltaic (CPV) system [23], solar panels [24] or solar-pumped lasers [25–27], (Fig. 8.5). In 2012, a high accuracy solar tracking system was developed which achieved 0.01%

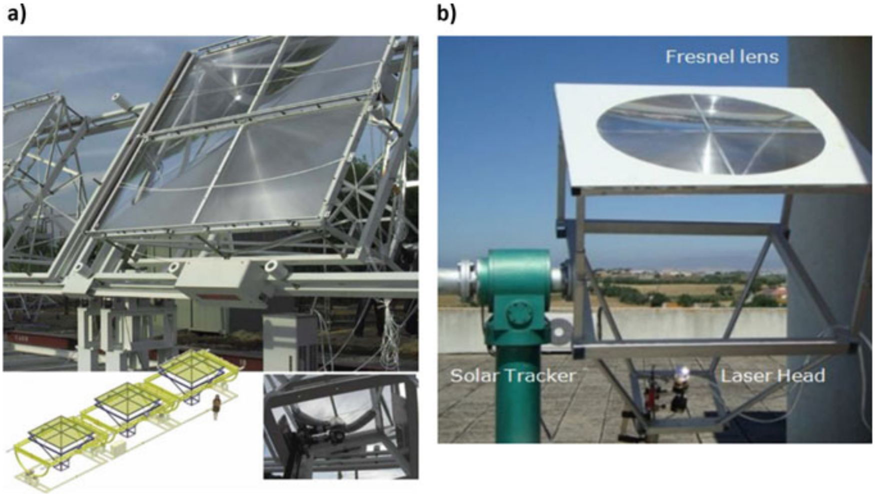

Fig. 8.5 Solar-pumped laser setups using Fresnel lenses and direct solar tracking systems from [25, 27]

standard deviation between the simulated and measured values of the available solar radiation [28].

The conclusion is that double-axis STS always achieved good performances with greater efficiencies between 20 and 50% energy gains when compared to fixed flat panels and/or CSP systems [9]. In 2014, Yao proposed a multipurpose double-axis STS that can be applied to solar power systems. Results of the accuracy test indicate that the tracking error of the normal tracking strategy is within 0.15°. Furthermore, in the test on the output of the PV modules, it is found that the average energy efficiency of the normal tracking PV, compared with the fixed PV, is more than 23.6%, as shown in Fig. 8.6. The average energy efficiency of the daily adjusted PV is more than 31.8% [29].

The direct tracking mode has the advantage of higher solar irradiation upon the receiver, due to the primary collector being continuously pointed directly to the Sun, discarding another mirror while is in use. However, indirect tracking mode has the advantage of protecting the most expensive and sensible primary solar concentrator, altogether with the receiver and all components of the solar application inside an infrastructure, and a more stable solar energy delivery in any application.

8.3.2 *Indirect Solar Tracking Mode by Heliostats*

The contents in this section are classified in solar tracking systems which use heliostats whose track the Sun, reflecting the solar radiation toward the collector, as shown in Fig. 8.7.

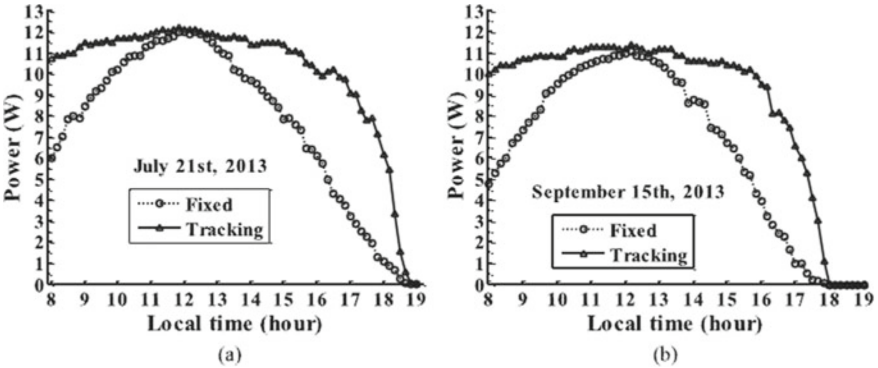

Fig. 8.6 Output of the normal tracking and fixed PV module on the days of **a** July 21st; **b** September 15th [29]

Fig. 8.7 Photograph of a heliostat tracking the Sun and reflecting the solar radiation to a medium size parabolic mirror in Almeria solar plant, Spain

Since the first STS, introduced in 1962 [30] using single heliostats, showing very little increased performance over fixed systems, many other researchers have investigated solar trackers in order to improve their solar collection efficiency [31, 32], with the tracking error tolerances varying between 0.5° and 1°. Significant improvement on the accuracy of STS was noticed since 1985, after Badescu et al. demonstrated the influence of the astronomical and constructive parameters on the concentration of solar radiation with plane heliostats on the tracking surfaces of PV systems [33]. Solutions were investigated to correct the heliostat offset errors and the reflected solar radiation images to the receiver using cameras. The system had a digital camera capturing the real time Sun images projected by the heliostats and supplied it to the computer. These images were then compared to the inbuilt reference images where the solar radiations were perpendicular to the heliostat. The difference between these two images generated a control signal which was used by the control system to activate the servo-motors and reorient the collector back to 90° with respect to the solar radiation beam [34]. Chen in 2005 derived general Sun tracking formula for heliostats with arbitrarily oriented axes [35].

A solar double axis tracker was developed in 2007, with a higher concentration of solar energy using a tracking master mirror surrounded by several other slave mirrors, which reflected collected solar radiation onto a stationary target. The solar image reflected by the master mirror was used as a reference for all slave mirrors. The rotational axis was configured pointing to the target and the other one was the elevation axis parallel to the reflector [36]. Using two photo-sensors and a heliostat, reflecting the solar radiation to a 70 m away target screen, system's tracking error was evaluated at 0.11° in a clear weather [37]. In 2014, a beam characterization system was used to evaluate the tracking error of two heliostats from a central tower solar plant with an estimated accuracy of about 2% for the positioning angle measurement [38].

For extremely high inputs of radiant energy, a multiplicity of flat mirrors, or heliostats, using altitude-azimuth mounts can be used to reflect their incident direct solar radiation onto a common target, as shown in Fig. 8.8. This is called the heliostat field or central receiver collector. The heliostat field typically represents 30–50% of the capital cost of the system and the required size of the heliostat field for a given nominal power of a solar plant is reduced with an increased optical efficiency. Similarly, increasing thermal performance of the receiver decreases the required size of the heliostat field and the associated capital cost [39].

Central receivers have several advantages [40]:

Fig. 8.8 Photograph of a large parabolic mirror in PROMES CNRS, France: the heliostat field reflects their incident direct solar radiation onto a parabolic mirror, which concentrates the solar radiation onto a target at its focal zone

1. They collect solar energy and transfer it to a single receiver, thus minimizing thermal energy transport requirements.
2. They typically achieve concentration ratios of 300–1500 and so are highly efficient.
3. They can conveniently store thermal energy.
4. They are quite large (generally more than 10 MW) and thus benefit from economies of scale.

The heliostats collect and concentrate Sunlight onto the receiver, which absorbs the concentrated solar energy, transferring its energy to a heat transfer fluid. A thermal storage system typically stores the collected energy as sensible heat for later delivery to the power conversion system.

8.4 Tracking Error in Different Primary Solar Concentrators

8.4.1 Solar Tracking Error in Parabolic Mirrors

Solar concentration systems as point-focusing concentrators need to employ some form of solar tracking mechanism with sufficient accuracy [41], usually with less than 0.05° [15, 42], for enabling the achievement of higher concentration ratios, radiation flux and thus conversion efficiency [1]. Consequently, it becomes necessary to follow the daily apparent motion of the sun in both altitude and azimuth directions, requiring a solar tracking system [1, 43]. Parabolic collectors generally use a method in which the sun tracker moves in both altitude and azimuth direction.

Parabolic trough collectors (PTCs) generally use a one-axis tracking system, which follows the sun in only one direction. PTCs are a well established solar energy technology, implemented in many places to produce electricity via solar cells or thermal processes. Significant advancements have been demonstrated in the last decades with several approaches and strategies to increase the output power harvested from these collectors [44–46]. 68.8% higher in heat gain achieving 15–17% more in collector efficiency or an enhanced optical efficiency of 0.81% were obtained using double-axis STS [47, 48]. Solar tracking systems have been also developed in order to improve the solar collection and concentration efficiency of parabolic dish solar concentrators, which have attracted much interest for many researchers, as a mean to reach high concentration ratios [10, 49–51]. In 2019, Natarajan et al. obtained 86% of short circuit current value of the concentrated panel compared with conventional PV panel [52].

In Fig. 8.8a is shown a two-axis heliostat and a stationary parabolic mirror with 1.5 m diameter, 60° rim angle and 660 mm focal length and its two axis of rotation. It also shown in Fig. 8.9b the position of the focal spot at its optimal alignment, in the absence of solar tracking error, and in two extreme cases for the maximum solar tracking errors of $\Delta Y = 0.3°$ and $\Delta X = 0.3°$.

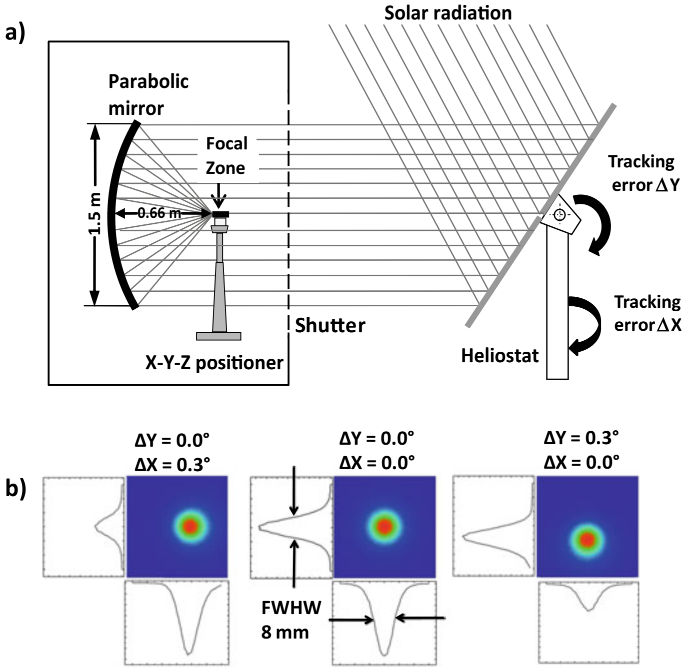

Fig. 8.9 **a** Schematics of a heliostat-parabolic solar energy collection and concentration system and the heliostat orientation error direction at ΔY and ΔX. **b** The focal spot of the parabolic mirror at its optimal alignment, in the absence of solar tracking error and at two extreme cases for solar tracking errors of $\Delta X = 0.3^\circ$ and $\Delta Y = 0.3^\circ$

Motohiro, aiming to attain efficient solar energy conversion to laser light and utilizing originally designed μSPLs, developed a precise direct solar tracking system with an error smaller than 0.06°, required because of the high concentration ratio: 1 = 10626 of the μSPL collector mirror. Thus, a prototype system with precision < 0.06° for 25 μSPLs in an array was successfully fabricated in that study.

Studying the tracking error influence in solar lasers with two types of secondary concentrators, cylindrical and aspherical at the focus of a parabolic dish, Tiburcio et al. [53, 54], have numerically investigated the solar laser output power using a dual-rod scheme as a function of the tracking errors, in order to develop a tracking error compensation capacity solar laser scheme. The tracking error width at 10% laser power loss ($\text{TEW}_{10\%}$) was chosen to analyze the tracking error compensation capacity of the schemes. For a fused silica cylindrical lens as a secondary concentrator, a large improvement in tracking error compensation capacity was numerically attained with that approach, leading to 2.57 and 3.00 times enhancement in tracking error width at 10% laser power loss in ΔY (altitude) and ΔX (azimuth) errors, respectively, as compared to the most efficient end-side-pumped scheme by the same collection area. Using aspherical fused silica lens as a secondary concentrator, this results were improved with, where the $\text{TEW}_{10\%}$ was improved 1.66 and 1.21 times at altitude

(ΔY) and azimuth (ΔX) tracking errors, respectively, as compared to the numerically simulated side-pumped single-rod scheme. In 2022, the first experimental results of tracking error compensation capacity of a solar-pumped laser pump by a heliostat-parabolic mirror were demonstrated, which it will be given in Sect. 8.5.2.1 [55].

8.4.2 Solar Tracking Error in Fresnel Lenses

In the field of concentrated solar energy applications, Fresnel lenses have been one of the best choices because of the advantages such as small volume, light-weight, mass production with low cost, despite the chromatic aberration that is produced at the focus [56]. Point-focus concentrating systems with azimuth-elevation tracking can obtain a high energy density and overall efficiency, but, in return, this results in an increase in the initial and operational costs. Compared with the azimuth-elevation tracking, the advantage of polar-axis tracking is the best one-axis tracker, delivering around 97% of the yearly energy of azimuth-elevation trackers, and its cost is approximately half that of the azimuth-elevation one [2].

Several researchers have studied and developed STS for Fresnel lens concentrators over the years [57–62]. Yabe et al. proposed a solar laser system that uses the Fresnel lens with a double-axis direct tracking system to demonstrate a fossil-fuel-free energy cycle with magnesium and laser [63, 64]. Perini presented a model for a novel linear Fresnel lens collector with dual-axis tracking capability, where the optical and thermal models of the Fresnel lens collector with 2D tracking are presented and validated using experimental data. The conclusion was that both single and dual axis tracking remain an option [65].

Liang et al. improved several times the solar-pumped laser efficiency using a Fresnel lenses with a double-axis direct tracking system, presented in Fig. 8.10 [25, 26].

8.4.3 Solar Tracking Error in Ring-Array Concentrators

A ring-array solar concentrator, introduced and developed by Vasylyev et al. [66] consists of a set of concentric rings disposed in such way that the inner reflective surfaces do not mutually shade, shaping its focal spot through superposition of rays to a common point in the rear side of the collector, as shown in Fig. 8.11. This configuration allows efficient integration of components, decreasing the shadow areas between incoming solar rays and the laser head, as compared with heliostat-parabolic mirror.

In 2018, it was studied a typical tracking error from 0.05° to 0.2° in either azimuthal and altitude axes through the laser output power variation. Figure 8.11 represents the RAC designed in [67], which is composed of 13 rings, each with off-axis parabolic profile, 0.6 mm thickness and protective-silver coated with 95% reflectivity. In the

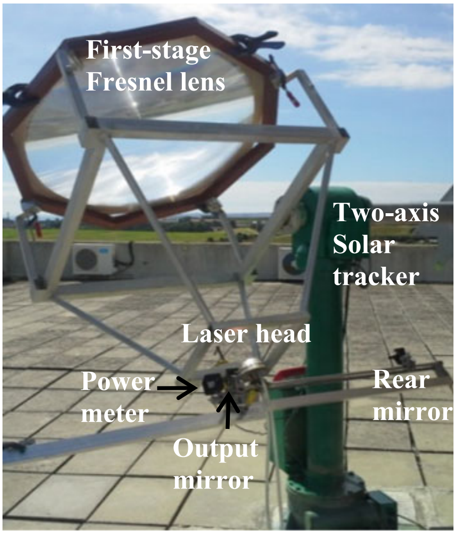

Fig. 8.10 The solar-pumped Nd:YAG solar laser system from [26]

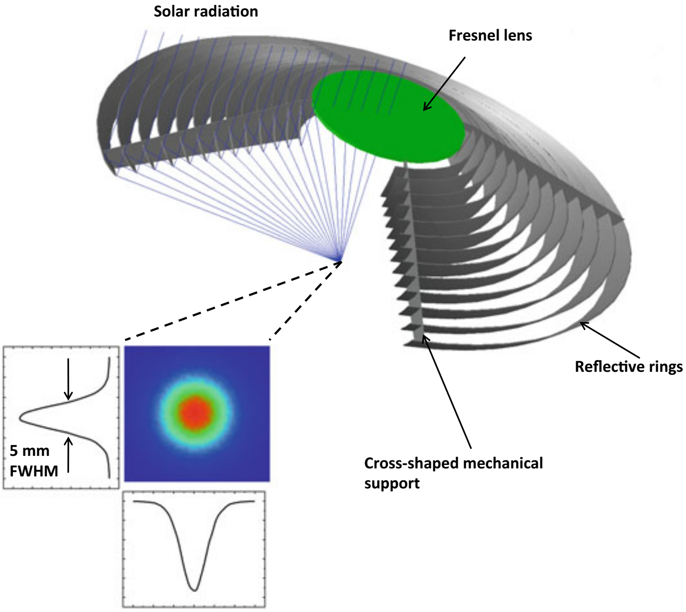

Fig. 8.11 The ring-array concentrator is composed of 13 rings and a small Fresnel lens. Inset picture with the pump light distribution at its focal point

central region of the RAC a small Fresnel lens is also mounted. A mechanical structure connecting all these rings and the Fresnel lens is also given in Fig. 8.11. The influence of tracking error on the output laser power for the 5.0 mm diameter, 20 mm length Nd:YAG rod was studied. At the maximum tracking error of 0.2° in both azimuth and altitude axes, 48.5 W was attained, corresponding to 28% laser power loss, using an end-side-pumping scheme. De Matos et al. proposed in 2018 a modified RAC [68]. It was studied a typical tracking error from 0.05° to 0.20° in either azimuthal and altitude axes. At the maximum tracking error of 0.2° in both azimuth and altitude axes, 50.4 W was attained, corresponding to 25.7% laser power loss. To correctly evaluate the tracking error associated laser output power, a 1.5 m diameter Fresnel lens was also designed to pump the same 5.0 mm diameter 20 mm length Nd:YAG rod. Therefore, a very clear advantage of the modified ring-array system in both solar laser output power enhancement and tracking error associated laser power reduction was demonstrated in comparison to Fresnel lenses.

Garcia et al. analyzed is the efficiency loss of the spherical receiver of 15 mm diameter as function of tracking error in altitude and azimuth directions for MSSF parabolic mirror and 3D RAC solar furnace [69]. At the extreme case of tracking error by 0.5° on both axes, the efficiency was nearly extinguished for the MSSF parabolic mirror and a 60% loss was obtained for 3D RAC. Tiburcio et al. studied the same RAC designed before to investigate the dual-rod side-pumping concept as an interesting alternative to attain an improved solar laser output power, with better beam quality and tracking error compensation capacity [70]. In Fig. 8.12 is shown the 3D normalized solar laser power for both the single and the dual-rod side-pumping schemes from this work and the end-side-pumping scheme from reference [71], as a function of the simultaneous altitude and azimuth solar tracking errors ranging from 0.0° to 0.3°.

The influence of tracking error on RAC side-pumping solar laser performance was also investigated, showing only 2% power loss for a tracking error of 0.1° at altitude and azimuth directions simultaneously. The dual-rod side-pumping concept is an interesting alternative to attain an improved solar laser output power with better beam quality and tracking error compensation capacity, comparatively not only with the single-rod side-pumping scheme but also with the end-side-pumping scheme from [71]. The significant improvement in the thermal performance of the laser media helps to increase the laser performance and stability.

8.5 Tracking Error Compensation Techniques

8.5.1 Monolithic Fused Silica Twisted Light Guide

In order to improve the overall stability and tracking error tolerance on solar lasers, in 2008 Geraldes et al. designed and simulated nine fused silica light guides of square cross-section are used to form the light guide assembly, as shown in Fig. 8.13 [72].

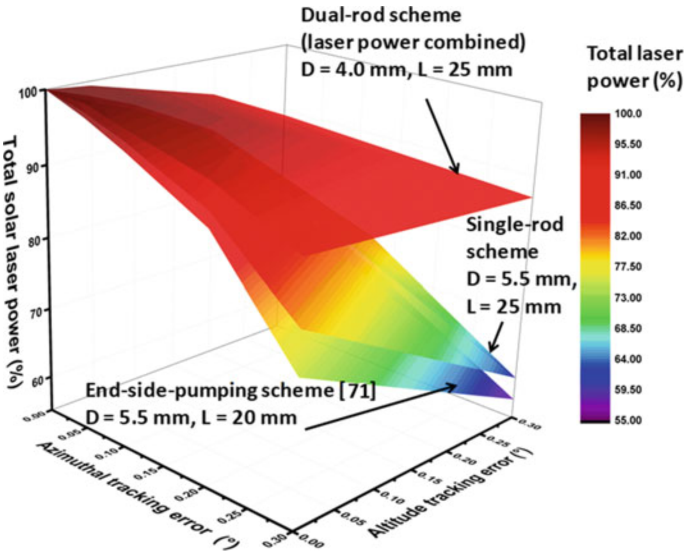

Fig. 8.12 The normalized total solar laser output power in percentage, for both the single and the dual-rod side-pumping schemes, and the end-side pumping scheme [71], as a function of the simultaneous variation in altitude and azimuth solar tracking errors, ranging from the optimal alignment (0.0°) to 0.3°, using the same RAC solar energy collection and concentration system

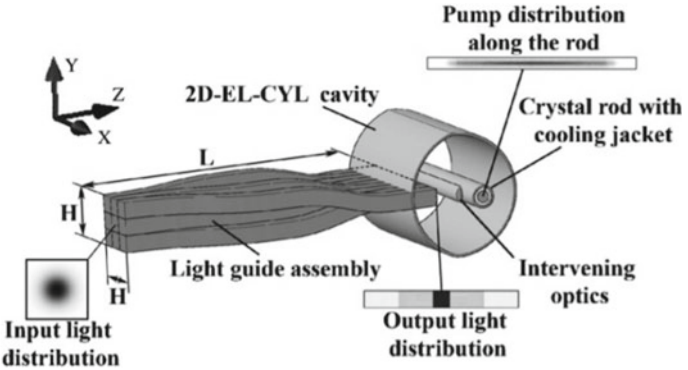

Fig. 8.13 Light guide assembly 2D-CYL-EL cavity with intervening optics. End plates have been removed for better illustration

The input ends of the light guides were packed together to form a 20 × 20 mm^2 square input face. The input face of the assembly is placed at the focal spot of the primary mirror and the output end coupled to the first focal line of the 2D-ELCYL cavity. Figure 8.14a shows both the input and output pump light distributions of the light guide assembly, corresponding to the optimum alignment between the heliostat and the primary parabolic concentrator. For the combined tracking errors in XY-axes, the focal spot is located near the center of the four upper left light guides, resulting in the strongly shifted output distribution as given in Fig. 8.14d.

In 2017, a fused silica twisted light guide was experimentally simulated and tested with tracking error compensation capacity [73, 74]. The concentrated solar radiation was firstly collected by the twisted fused silica light guide with 16 mm 16 mm input face. It was then transmitted along 110 mm length, observing both refraction and total internal reflection principles, to its rectangular output end with 8.0 mm, 32 mm, as illustrated in Fig. 8.15. The near-Gaussian profile of the concentrated light spot incident on the input face of the light guide assembly was therefore transformed into a rectangular pump light column at the assembly output end.

For the combined tracking errors of 0.2° in both X and Y axes, the focal spot was shifted obliquely from the center of the input face of the lower straight part of the light guide, causing a reduction in laser output power and a modification of the fundamental mode beam profile.

8.5.2 Multi-Rod Pumping Approach

8.5.2.1 Multi-Rod Pumped Through a Fused Silica Cylindrical Secondary Concentrator

Multi-rod concepts have been numerically investigated using different secondary concentrators in order to improve the solar laser emission stability and tracking error compensation capacity. Tiburcio et al. in 2019 had numerically investigated a cylindrical concentrator in a dual-rod side-pumping configuration [53]. The tracking error of the optimized dual and single-rod schemes was firstly studied and then was compared to that of the most efficient end-side-pumped laser [71]. All these schemes were pumped by NOVA heliostat-parabolic solar collection and concentration system with the same collection area of 1.56 m^2. The tracking error width at 10% laser power loss ($TEW_{10\%}$) was chosen to evaluate the tracking error compensation capacity of the schemes.

In Fig. 8.16 is shown the influence of the solar tracking error on the dual-rod scheme in altitude (ΔY) and azimuth (ΔX) directions. With the tracking error at ΔY, the focal spot moved upwards (Fig. 8.16a), from the lower rod to the upper rod in the dual-rod scheme. With the tracking error at ΔX, the focal spot moved in the azimuthal direction of the dual-rod scheme (Fig. 8.16b). With the simultaneous tracking error in ΔY and ΔX, the focal spot moved upwards to the upper rod and also to the right in azimuthal directions (Fig. 8.16c).

In Fig. 8.17 is shown the absorbed pump flux distribution along the longitudinal cross-section of the dual-rod and the single-rod pumped with solar tracking error at ΔY, ΔX and ΔY and ΔX, simultaneously. The laser output powers are also indicated.

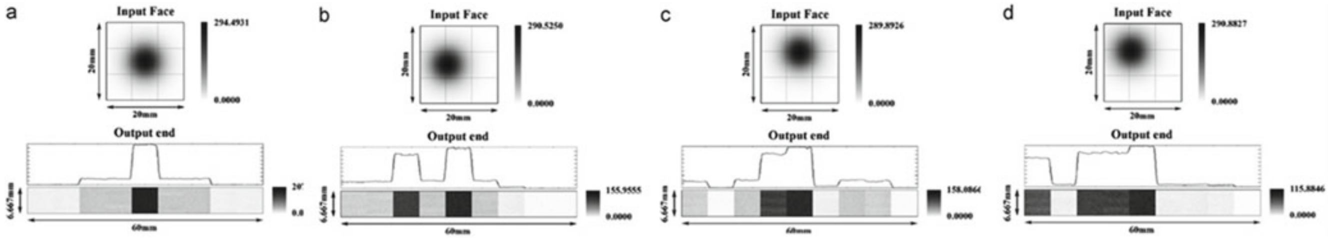

Fig. 8.14 Input and output light distributions for the cases of **a** zero tracking error, **b** *X*-axis 3 mm displacement, **c** Y-axis 3 mm displacement and **d** combined X–Y axes 3 mm displacement

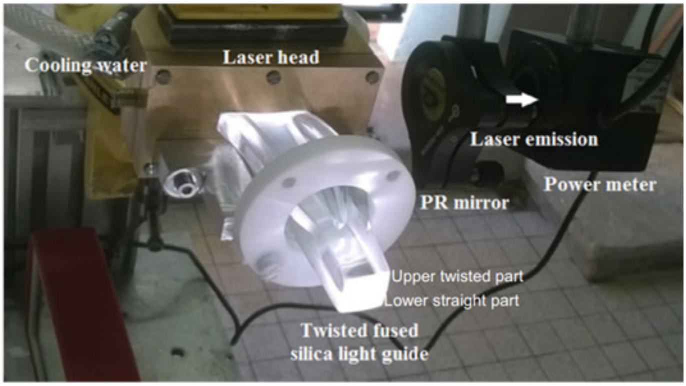

Fig. 8.15 Solar-pumped Nd:YAG laser head composed of the monolithic light guide, the solar laser head and the laser resonant cavity [73]

8.5.2.2 Multi-Rod Pumped Through a Fused Silica Aspherical Secondary Concentrator

The single and the dual-rod schemes were studied regarding to the tracking error capacity using an aspherical lens as a secondary concentrator [54]. In Fig. 8.18 is shown an example of the influence of the solar tracking error on the dual-rod scheme in altitude (ΔY) and azimuth (ΔX) directions individually, and at ΔY and ΔX directions simultaneously. With the tracking error at only ΔY, the focal spot moved upwards, from the lower rod to the upper rod (Fig. 8.18a). With the tracking error at ΔX, the focal spot moved along the laser rods (Fig. 8.18b). With the simultaneous tracking error in ΔY and ΔX, the focal spot moved upwards to the upper rod and also to the right (Fig. 8.18c).

The normalized total multimode laser output power as a function of the ΔY and ΔX solar tracking errors (from the optimal alignment to 0.35° tracking error) for both the single and the dual-rod schemes and also for the 3.5 mm diameter, 25 mm length Nd:YAG from the previous dual-rod scheme are shown in Fig. 8.19 [53].

In 2022, the first experimental results of tracking error compensation capacity of a solar-pumped laser were demonstrated, with a largely enhanced tracking error tolerance achieved by pumping two laser rods simultaneously [55]. A large aspherical fused silica lens, with an input face of 46 mm radius of curvature and 84 mm diameter, provided an efficient focusing of the concentrated solar radiation from the focal spot of the parabolic mirror onto the two laser rods, mounted within two semicylindrical pump cavities.

In Fig. 8.20 is presented a photograph of the dual-rod solar laser head and the two laser power meters used to measure the solar laser output powers from each one of the rods.

The altitude h and the azimuthal α position of the Sun were calculated in two moments during the experiment: when the system was optimally aligned (t_0), and

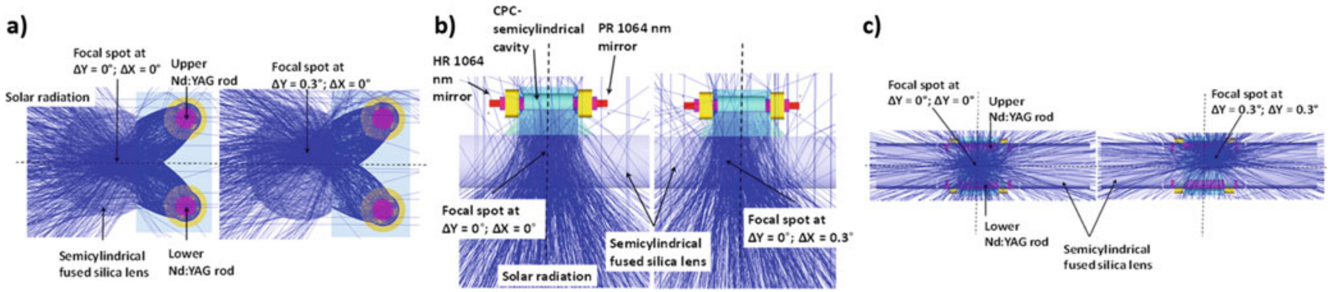

Fig. 8.16 The Influence of the solar tracking error in the focal spot to pump the dual-rod scheme at **a** ΔY, moving upwards from the lower rod to the upper rod; **b** ΔX, moving in azimuthal direction; **c** ΔY and ΔX simultaneously, moving the focal spot upwards to the upper rod and also to the right in azimuthal direction

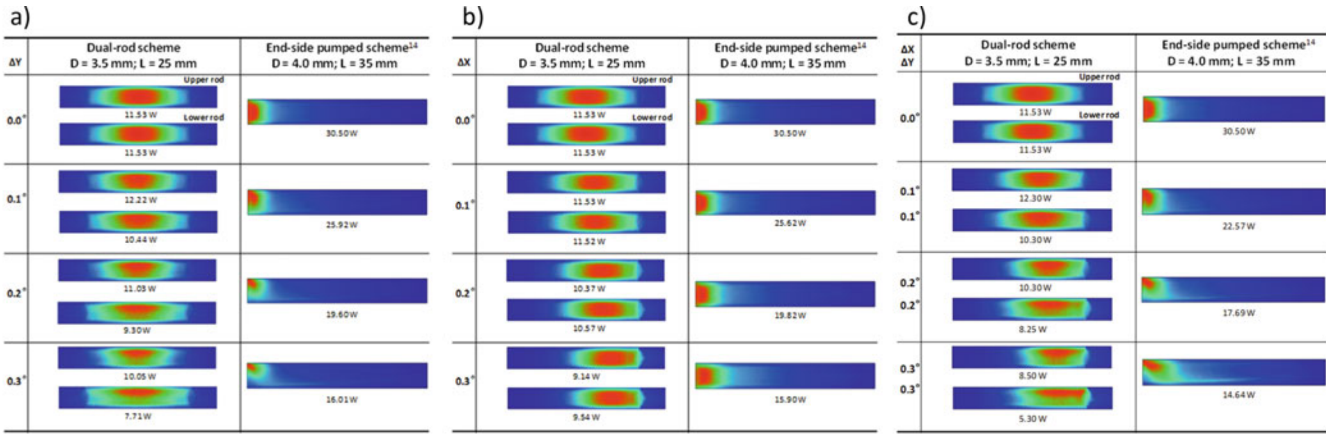

Fig. 8.17 The absorbed pump flux distribution along the longitudinal cross-section of the Nd:YAG crystal rods, pumped with solar tracking error at **a** ΔY, **b** ΔX and **c** ΔY and ΔX simultaneously, for the dual-rod and the end-pumped scheme [71], with the same collection area of NOVA solar system. The numerically obtained laser output powers are also indicated

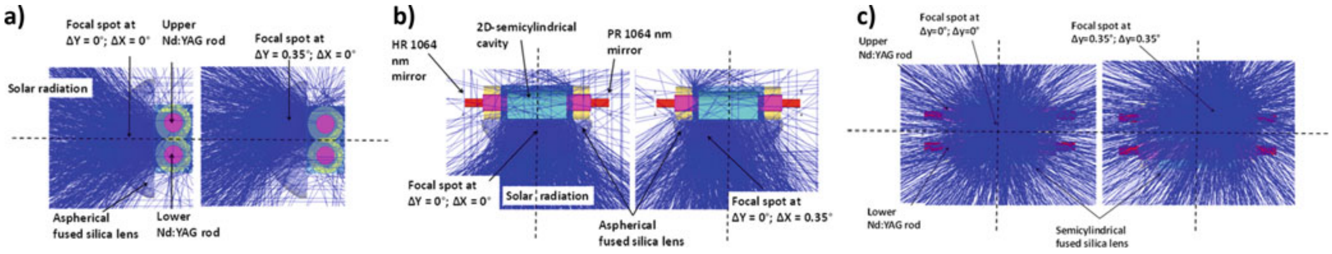

Fig. 8.18 Solar tracking error and its influence in the focal spot to pump the dual-rod scheme at **a** altitude direction (ΔY), **b** azimuth direction (ΔX) and **c** ΔY and ΔX simultaneously

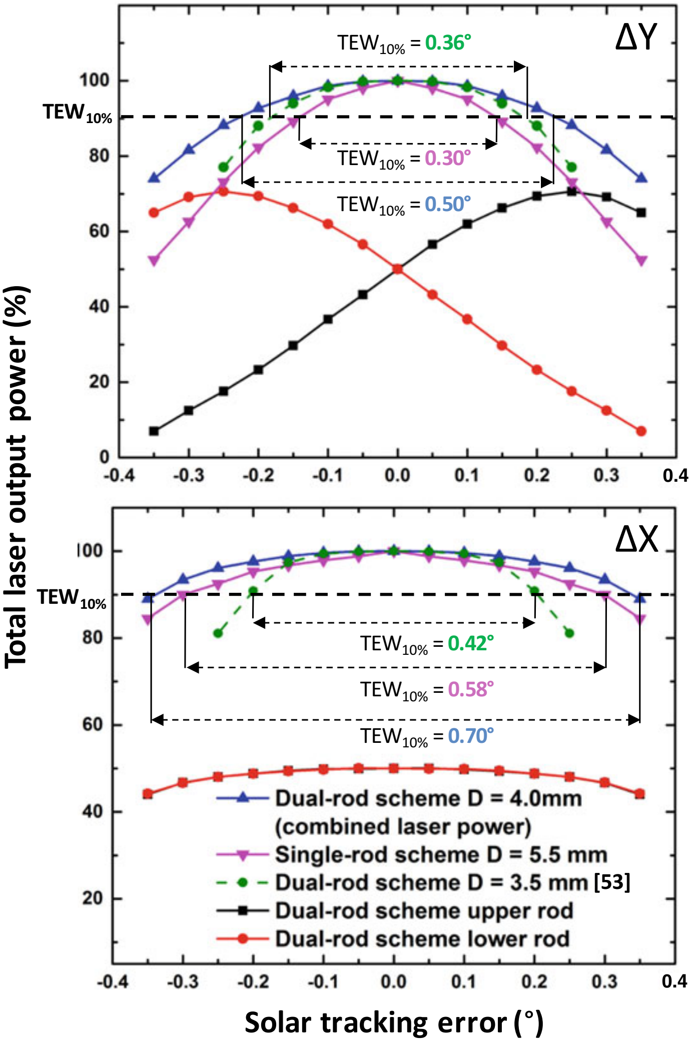

Fig. 8.19 Normalized total multimode laser output power, from the optimal alignment (0.0°) of the solar laser head, as a function of the ΔY and ΔX solar tracking errors, for the single and the dual-rod schemes and also for the previous dual-rod scheme [53]. It is also shown the normalized power for each laser rod from the dual-rod scheme (both upper and lower rod), as well the tracking error width at 10% laser power loss ($\text{TEW}_{10\%}$)

after one minute (t_1), with the heliostat stopped [1]. The dual-rod side-pumping tracking error compensation capacity was tested using two setups: one vertical (i.e. the solar laser beams emitted vertically), and one horizontal (the laser beams emitted horizontally). In Fig. 8.21 is shown the solar laser head and the schematics for two maximum displacements of the focal spot, due to the solar tracking error in both

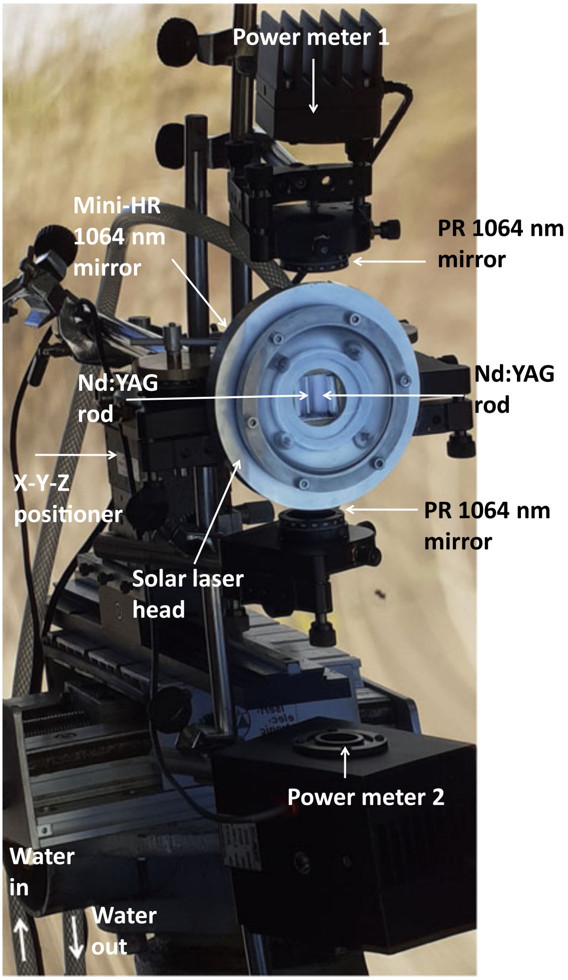

Fig. 8.20 Photograph of the solar laser head showing the two Nd:YAG rods, the water cooling scheme, the laser resonator mirrors and the laser power meters 1 and 2

altitude and azimuth directions are presented, corresponding to the positions 1 and 3 in Fig. 8.21a–c, respectively. The optimal alignment is represented by the position 2 in Fig. 8.21b. In Fig. 8.21d is shown the normalized total solar laser power from the left and the right laser rods, as well as the normalized solar laser power from each rod.

With the tracking error in altitude, the pump flux distribution moved only slightly along the laser rods of the dual-rod scheme. The largest tracking error occurred in the azimuth direction, which displaced the pump flux distribution from the left rod to the right rod. In Fig. 8.22 is presented the solar laser head and the schematics for two maximum displacements of the focal spot due to the solar tracking error in both altitude and azimuth directions in the horizontal setup, corresponding to the positions 1 and 3 in the Fig. 8.22a–c, respectively. The optimal alignment corresponds to the

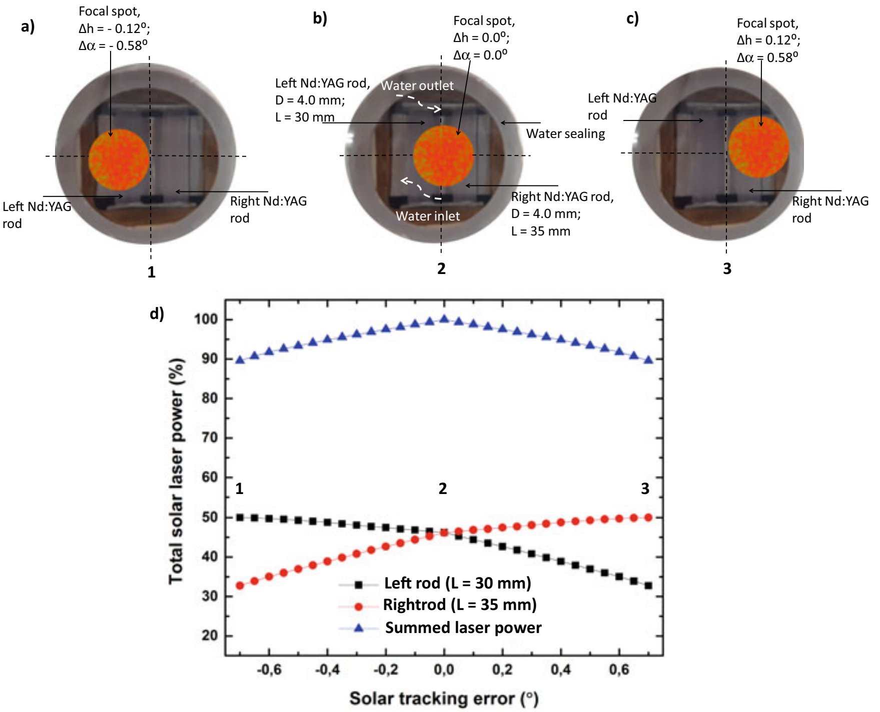

Fig. 8.21 The solar laser head and the schematics for **a**, **c** two maximum displacements of the focal spot due to the solar tracking error in both altitude and azimuth directions in the vertical setup, corresponding to the positions 1 and 3; **b** optimal alignment of the focal spot, corresponding to the position 2; **d** normalized total solar laser power for the left and the right laser rods

position 2 in Fig. 8.22b. In Fig. 8.22d is shown the normalized total solar laser power from the upper and the lower laser rods, as well as the normalized laser power from each laser rod. With the tracking error in altitude, the pump flux distribution moved from the lower rod to the upper rod of the dual-rod scheme. The tracking error in azimuth displaced the pump flux distribution along the rods.

The dual-rod side-pumping experiments resulted in a largely enhanced tracking error tolerance, as shown in Fig. 8.23, where the vertical and the horizontal setups presented a $\mathrm{TEW}_{10\%}$ of 1.4° and 0.6°, respectively, and a more stable solar laser emission as compared to the numerical models from a previous dual-rod scheme [54].

In comparison with the other numerical dual-rod side-pumping solar laser, with cylindrical lens and one pump cavity to each one of the laser rods in a horizontal setup [53], the experimental dual-rod side-pumping had also shown a significantly improved tracking error stability, as given in Fig. 8.24. The comparison with

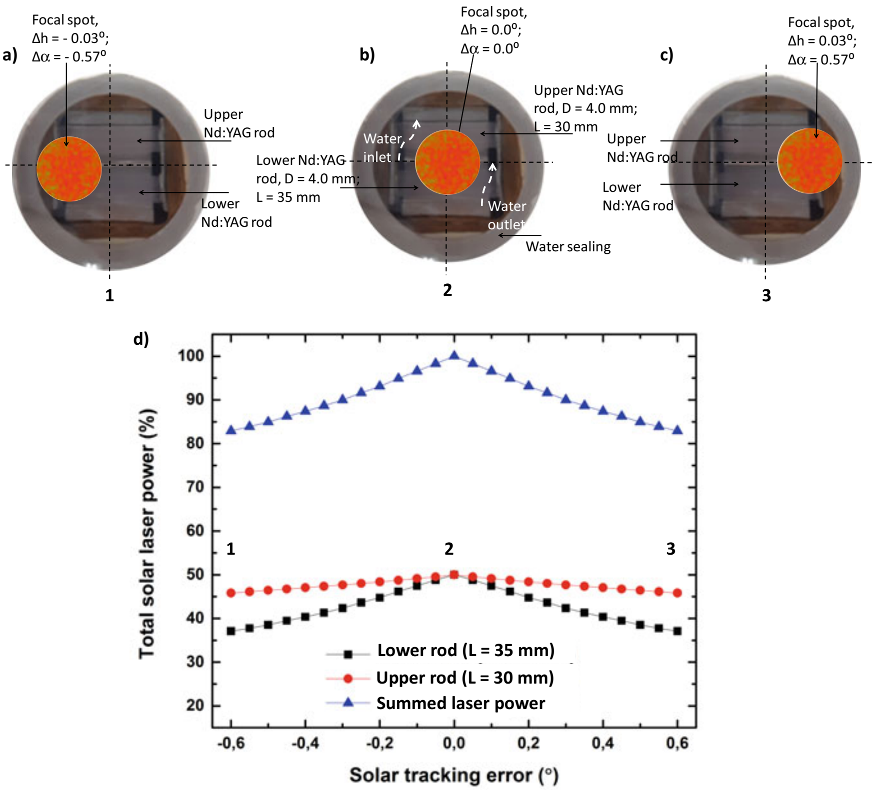

Fig. 8.22 The solar laser head and the schematics for **a**, **c** two maximum displacements of the focal spot due to the solar tracking error in both altitude and azimuth directions in the horizontal setup, corresponding to the positions 1 and 3; **b** optimal alignment, corresponding to the position 2; **d** normalized total solar laser power for the upper and the lower laser rods, as well as the normalized laser power from each laser rod

the numerically calculated tracking error compensation capacity of the most efficient experimental solar-pumped laser in an end-side-pumping configuration is also represented [53, 71].

Both the vertical and the horizontal setups had shown a substantially improved tracking error tolerance, providing a stable solar laser emission, even with large tracking error displacements of the focal spot.

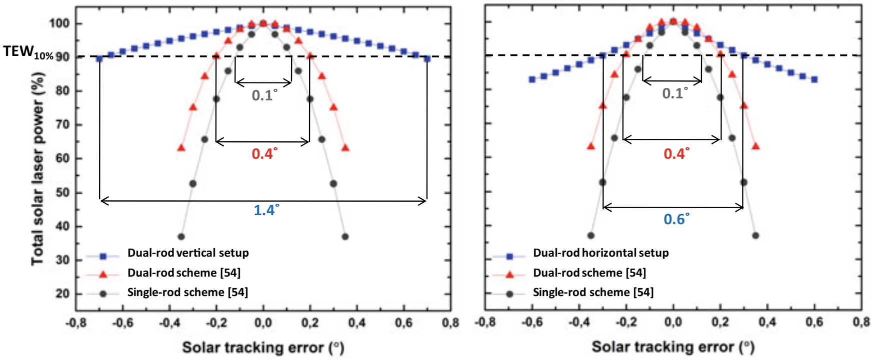

Fig. 8.23 Normalized solar laser output power from the vertical and horizontal setups with no Sun tracking, compared to the previous numerical results of the single-rod and the dual-rod side-pumping using a small aspherical lens as secondary concentrator [54]

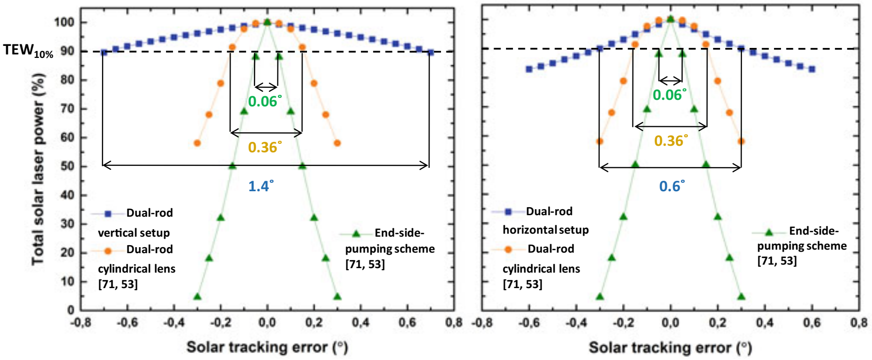

Fig. 8.24 Normalized solar laser output power with vertical and horizontal setups with no Sun tracking, compared to the previous numerical results of the solar laser approach using cylindrical lens as secondary concentrator [53], and that of the most efficient end-side-pumping solar laser [53, 71]

8.6 Example of Numerical Modeling of Solar-Pumped Lasers with Tracking Error Compensation Capacity

8.6.1 Zemax® and LASCAD™ Analysis of the Tracking Error Compensation Capacity Using Multi-Rod Configurations

In this section, it will be given an example, based on modeling in Zemax® and LASCAD™ software, of numerical tracking error compensation capacity using a multi-rod configuration with fused silica aspherical lens. Non-sequential ray-tracing is performed in Zemax® to analyze both the absorption efficiencies and the absorbed pump distributions within the Nd:YAG laser rod, then this information is exported to LASCAD™ in order to analyze the solar laser output and its dependency on the solar tracking error generated.

First, the primary solar concentrator composed of heliostat-parabolic mirror combined need to be programmed. The heliostat tracks the Sun continuously and reflects the solar radiation to the primary parabolic mirror. The combined reflectivity of the two reflective mirrors can be assumed as 80%, and this combined heliostat-parabolic system will be modeled to investigate a variation on the solar pumping based on the variation of the Sun's position. The primary mirror has 1.3 m diameter, 60° rim angle, 655 mm focal distance and 1.33 m^2 collection area. The divergence of the solar rays between [30000, 40000] can be assumed for the circular source to simulate the incoming solar radiation in Zemax® ray-tracing software, depending of the diffusivity. Considering 950 W/m^2 terrestrial solar irradiation, the concentrated light spot at the focus of the primary mirror can reach 1264 W.

In order to carry out the solar tracking error study of this solar laser system, the altitude and azimuth variations from the optimally aligned solar laser system to a certain amount of time need to be defined. For this case, the equations given in the Sect. 8.1.1 can be used, choosing a specific day and time of measurement, so that the other variables can also be determined to have a real coordinate variation for the tracking error study of the solar laser system. Alternatively, a solar position computer software, or algorithm, for tracing the sun is available as open source codes on internet. As an example, it is presented a table with calculated values for a given day and time of measurement, from [55]. In this way determining the values to be introduced in the X and Y tilt variations of the light source on Zemax® software for the simulations. In Table 8.1 is given time of measurement, latitude, declination, hour angle, azimuth and altitude variations in the Sun's position along one minute for August 18.

The dual-rod solar-pumped laser can be studied as an example of multi-rod configuration, assembled with a large fused silica aspherical lens as a secondary concentrator. Figure 8.25 gives the key dimensions of the Zemax® simulation model to be numerically tested.

Using the Table 8.1 and the values for the tracking error and solar irradiation conditions, the dual-rod horizontal scheme can be tested for tracking error compensation

Table 8.1 Values used for the calculation of the variation in the Sun's position along one minute for August 18, for the two dual-rod configurations used in the experimental measurements in [55]

Variables	Values (°)	
	t_0	t_1
$\varphi(°)$	38	38
$\delta(°)$	12.83	12.83
$\omega(°)$	12.25	12.50
$\Delta h(°)$	0.03	
$\Delta\alpha(°)$	0.57	

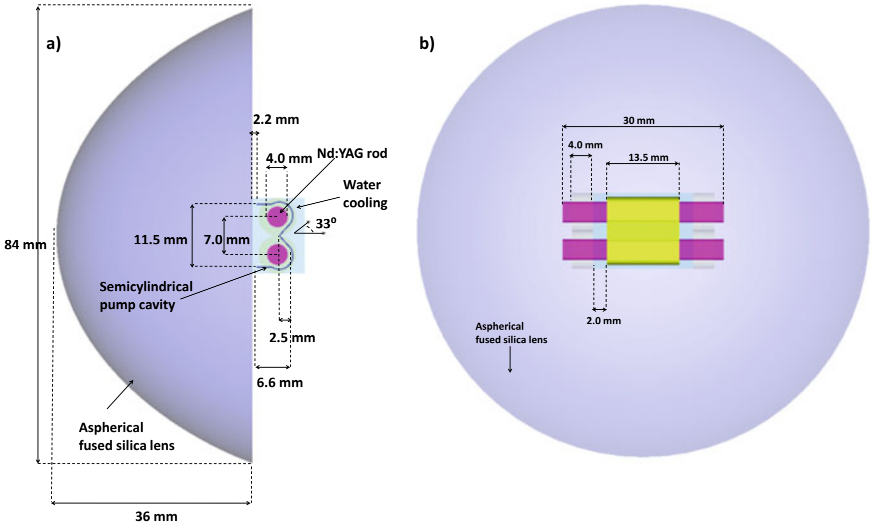

Fig. 8.25 **a** Front view of the solar laser head model of the Nd:YAG dual-rod side-pumping scheme and its key dimensions; **b** top view of the solar laser head

capacity, by inserting the calculated solar tracking errors at azimuth and altitude axis in the tilt about *X* and *Y* in the solar source of the Zemax® non-sequential component editor, respectively, simulating in this way a displacement on the solar pumping of the laser rods due to the displacement of the solar source in both axis. In the Fig. 8.26 is given the pump flux absorption distribution of the solar laser head model of the Nd:YAG dual-rod side-pumping scheme for the calculated solar tracking errors for August 18, around midday.

Alternatively, the vertical configuration can be also tested, by inserting the calculated solar tracking errors at azimuth and altitude axis in the tilt about *Y* and *X* in the solar source, respectively. In Fig. 8.26 is given the absorbed pump flux distribution along the longitudinal cross-sections of both the laser rods in Zemax® software, for the optimal alignment and two maximum displacements of the focal spot due to the solar tracking error in both altitude and azimuth directions, for the horizontal and vertical schemes. The larger tracking error in azimuth direction displaced the pump flux distribution along the rods for the horizontal scheme. In the case of the vertical scheme, the tracking error in azimuth direction displaced the pump flux distribution from the left/right rod to the right/left rod.

The laser resonant cavity analysis and optimization of the laser output power can be carried out using LASCAD™ software. Through the adoption of a symmetrical laser resonant cavity, the multimode solar laser output power can be efficiently extracted and analyzed. Different radius of curvature (RoC) and resonant cavity lengths can be studied for several rod diameters and lengths. The maximized numerical multimode solar laser output power for the dual-rod scheme was achieved with a 50 mm total length resonant cavity, being 10 mm as the separation lengths amongst

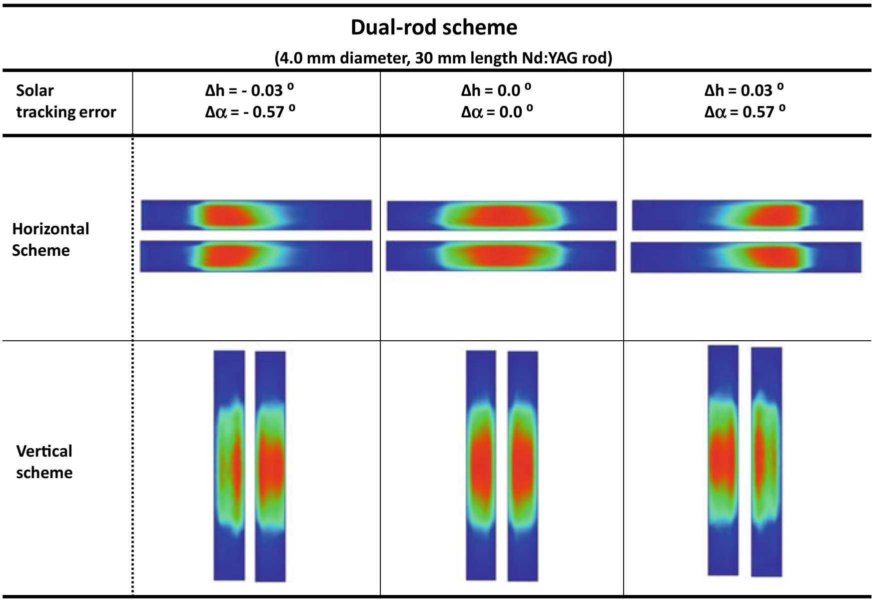

Fig. 8.26 Absorbed pump flux distribution along the longitudinal cross-sections of both the laser rods, for the optimal alignment ($\Delta h = 0.0^{\circ}$; $\Delta\alpha = 0.0^{\circ}$) and two maximum displacements ($\Delta h = 0.03^{\circ}$; $\Delta\alpha = 0.57^{\circ}$ and $\Delta h = -0.03^{\circ}$; $\Delta\alpha = -0.57^{\circ}$) of the focal spot due to the solar tracking error in both altitude and azimuth directions, for the horizontal and vertical schemes

the end-mirror and the output mirror to the end-faces of the laser rod, and RoC = −10 m for both mirrors, as shown in Fig. 8.27.

The solar laser output powers obtained for the tracking error study are presented in Table 8.2.

The Zemax® and LASCAD™ models presented in this section give numerical results which corresponds to the obtained experimental data from [55]. Other intermediate values of solar tracking error for that day can also be simulated, in this way

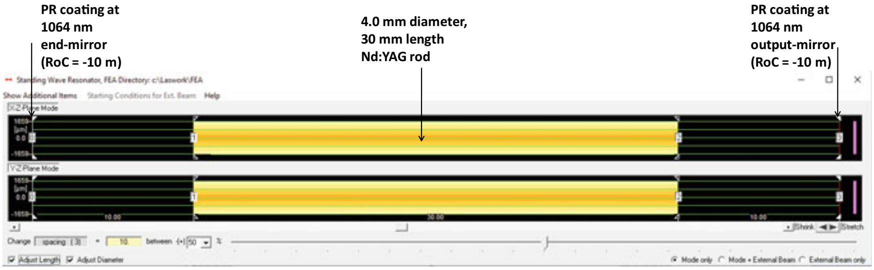

Fig. 8.27 Symmetric laser resonant cavity for the solar laser output power in LASCAD™ software: 10 mm was the separation lengths among the end-mirror and the output mirror to the end-faces of the laser rod. It is also indicated the RoC's used for the extraction of the solar laser

Table 8.2 Numerically calculated laser output power influenced by the calculated solar tracking errors for the dual-rod scheme in horizontal and vertical configurations

Solar tracking error (°)	Configurations					
	Dual-rod horizontal scheme			Dual-rod vertical scheme		
	Laser power (W)		Total power (W)	Laser power (W)		Total power (W)
	Nd:YAG Left rod	Nd:YAG Right rod		Nd:YAG Left rod	Nd:YAG Right rod	
$\Delta h = -0.03°$ $\Delta \alpha = -0.57°$	4.36	4.89	9.26	0.18	6.49	6.66
$\Delta h = 0.0°$ $\Delta \alpha = 0.0°$	6.91	6.92	13.83	6.91	6.92	13.83
$\Delta h = 0.03°$ $\Delta \alpha = 0.57°$	4.89	4.36	9.26	6.49	0.18	6.66

plotting a graph to determine the tracking error width at 10% for a given solar laser system for a specific day and time. Other experimental conditions for other days can also be simulated.

References

1. Kalogirou, S.: Solar Energy Engineering, vol. 1, 2nd edn. Academic Press, Massachusetts (2013)
2. Mousazadeh, H., Keyhani, A., Javadi, A., Mobli, H., Abrinia, K., Sharifi, A.: A review of principle and sun-tracking methods for maximizing solar systems output. Renew. Sustain. Energy Rev. **13**(8), 1800–1818 (2009). https://doi.org/10.1016/j.rser.2009.01.022
3. Hussein, M.T., Albarqouni, S.N.: Enhanced model of one axis-two positions manual tracking photovoltaic panels for lighting projects in Palestine. In: IASTED International Conference on Solar Energy 2010, pp. 15–17
4. Kreith, F., Kreider, J.F.: Principles of Solar Engineering (1978)
5. Duffie, J.A., Beckman, W.A.: Solar Engineering of Thermal Processes. Wiley, New York (1980)
6. Skouri, S., Ben Haj Ali, A., Bouadila, S., Ben Salah, M., Ben Nasrallah, S.: Design and construction of sun tracking systems for solar parabolic concentrator displacement. Renew Sustain Energy Rev **60**, 1419–1429 (2016). https://doi.org/10.1016/j.rser.2016.03.006
7. Poulek, V.: Testing the new solar tracker with shape memory alloy actors. In: Proceedings of 1994 IEEE 1st World Conference on Photovoltaic Energy Conversion-WCPEC (A Joint Conference of PVSC, PVSEC and PSEC), pp. 1131–1133. IEEE (1994)
8. Mwithiga, G., Kigo, S.N.: Performance of a solar dryer with limited sun tracking capability. J. Food Eng. **74**(2), 247–252 (2006). https://doi.org/10.1016/j.jfoodeng.2005.03.018
9. Nsengiyumva, W., Chen, S.G., Hu, L., Chen, X.: Recent advancements and challenges in solar tracking systems (STS): a review. Renew. Sustain. Energy Rev. **81**, 250–279 (2018). https://doi.org/10.1016/j.rser.2017.06.085
10. Agarwal, A.K.: Two axis tracking system for solar concentrators. (1992). https://doi.org/10.1016/0960-1481(92)90104-B
11. Abdallah, S., Nijmeh, S.: Two axes sun tracking system with PLC control. Energy Convers. Manage. **45**(11), 1931–1939 (2004). https://doi.org/10.1016/j.enconman.2003.10.007

12. Roth, P., Georgiev, A., Boudinov, H.: Design and construction of a system for sun-tracking. Renew. Energy **29**(3), 393–402 (2004). https://doi.org/10.1016/S0960-1481(03)00196-4
13. McCluney, R.: Passive optical solar tracking system. Appl. Opt. **22**(21), 3433–3439 (1983). https://doi.org/10.1364/AO.22.003433
14. Beshears, D.L., Capps, G.J., Earl, D.D., Jordan, J.K., Maxey, L.C., Muhs, J.D., Leonard, T.M.: Tracking Systems Evaluation for the Hybrid Lighting System. Paper presented at the ASME 2003 International Solar Energy Conference
15. Reda, I., Andreas, A.: Solar position algorithm for solar radiation applications. Sol. Energy **76**(5), 577–589 (2004). https://doi.org/10.1016/j.solener.2003.12.003
16. Baltas, P., Tortoreli, M., Russell, P.E.: Evaluation of power output for fixed and step tracking photovoltaic arrays. Sol. Energy **37**(2), 147–163 (1986). https://doi.org/10.1016/0038-092X(86)90072-1
17. Michaelides, I.M., Kalogirou, S.A., Chrysis, I., Roditis, G., Hadjiyianni, A., Kambezidis, H.D., Petrakis, M., Lykoudis, S., Adamopoulos, A.D.: Comparison of performance and cost effectiveness of solar water heaters at different collector tracking modes in Cyprus and Greece. Energy Convers. Manage. **40**(12), 1287–1303 (1999). https://doi.org/10.1016/S0196-8904(99)00020-5
18. Huang, B.J., Ding, W.L., Huang, Y.C.: Long-term field test of solar PV power generation using one-axis 3-position sun tracker. Sol. Energy **85**(9), 1935–1944 (2011). https://doi.org/10.1016/j.solener.2011.05.001
19. Chin, C.S., Babu, A., McBride, W.: Design, modeling and testing of a standalone single axis active solar tracker using MATLAB/Simulink. Renew. Energy **36**(11), 3075–3090 (2011). https://doi.org/10.1016/j.renene.2011.03.026
20. Kalogirou, S.A.: Design and construction of a one-axis sun-tracking system. Sol. Energy **57**(6), 465–469 (1996). https://doi.org/10.1016/S0038-092X(96)00135-1
21. Lazaroiu, G.C., Longo, M., Roscia, M., Pagano, M.: Comparative analysis of fixed and sun tracking low power PV systems considering energy consumption. Energy Convers. Manage. **92**, 143–148 (2015). https://doi.org/10.1016/j.enconman.2014.12.046
22. Yeh, P., Yeh, N.J.R.E.: Design and analysis of solar-tracking 2D Fresnel lens-based two staged, spectrum-splitting solar concentrators. **120**, 1–13 (2018).
23. Lv, H., Zheng, Y., Wang, J., Chen, B., Sheng, F., Cheng, C., Lv, Q.: Tracking control and output power optimization of a concentrator photovoltaic system with polar axis. Optik **127**(8), 3840–3843 (2016). https://doi.org/10.1016/j.ijleo.2016.01.092
24. Alexandru, C., Pozna, C.: Simulation of a dual-axis solar tracker for improving the performance of a photovoltaic panel. Proc. Inst. Mech. Eng., Part A: J. Power Energy **224**(6), 797–811 (2010). https://doi.org/10.1243/09576509JPE871
25. Liang, D., Almeida, J.: Highly efficient solar-pumped Nd:YAG laser. Opt. Express **19**(27), 26399–26405 (2011). https://doi.org/10.1364/oe.19.026399
26. Liang, D., Almeida, J.: Solar-pumped TEM_{00}-mode Nd:YAG laser. Opt. Express **21**(21), 25107–25112 (2013). https://doi.org/10.1364/oe.21.025107
27. Yabe, T., Bagheri, B., Ohkubo, T., Uchida, S., Yoshida, K., Funatsu, T., Oishi, T., Daito, K., Ishioka, M., Yasunaga, N., Sato, Y., Baasandash, C., Okamoto, Y., Yanagitani, K.: 100 W-class solar pumped laser for sustainable magnesium-hydrogen energy cycle. J. Appl. Phys. **104**(8), 083104 (2008). https://doi.org/10.1063/1.2998981
28. Missbach, T., Jaus, J.: New sensor for measuring tracking accuracy, tracker vibration, and structural deflection. AIP Conf. Proc. **1477**(1), 262–266 (2012). https://doi.org/10.1063/1.4753882
29. Yao, Y., Hu, Y., Gao, S., Yang, G., Du, J.: A multipurpose dual-axis solar tracker with two tracking strategies. Renew. Energy **72**, 88–98 (2014). https://doi.org/10.1016/j.renene.2014.07.002
30. Finster, C.J.S.: El heliostato de la Universidad santa maria. **119**, 5–20 (1962)
31. McFee, R.H.: Power collection reduction by mirror surface nonflatness and tracking error for a central receiver solar power system. Appl. Opt. **14**(7), 1493–1502 (1975). https://doi.org/10.1364/AO.14.001493

32. Semma, R.P., Imamura, M.S.: Sun tracking controller for multi-kW photovoltaic concentrator system. In, January 01, 1981 1981, p. 375
33. Badescu, V.: Influence of certain astronomical and constructive parameters on the concentration of solar radiation with plane heliostats fields. (1985)
34. Berenguel, M., Rubio, F.R., Valverde, A., Lara, P.J., Arahal, M.R., Camacho, E.F., López, M.: An artificial vision-based control system for automatic heliostat positioning offset correction in a central receiver solar power plant. Sol. Energy **76**(5), 563–575 (2004). https://doi.org/10.1016/j.solener.2003.12.006
35. Chen, Y.T., Lim, B.H., Lim, C.S.: General sun tracking formula for heliostats with arbitrarily oriented axes. J. Sol. Energy Eng. **128**(2), 245–250 (2005). https://doi.org/10.1115/1.2189868
36. Omar, A., Ismail, D., Muzamir, I., Mohd Rafi, A.: Simplification of sun tracking mode to gain high concentration solar energy. Am. J. Appl. Sci. **4**(3) (2007). https://doi.org/10.3844/ajassp.2007.171.175
37. Aiuchi, K., Yoshida, K., Onozaki, M., Katayama, Y., Nakamura, M., Nakamura, K.: Sensor-controlled heliostat with an equatorial mount. Sol. Energy **80**(9), 1089–1097 (2006). https://doi.org/10.1016/j.solener.2005.10.007
38. Sun, F., Wang, Z., Guo, M., Bai, F., Xu, Z.J.E.P.: Determination of tracking errors with respect to the geometrical errors based on optimization algorithm. Energy Procedia **49**, 2211–2220 (2014)
39. Pavlović, T.M., Radonjić, I.S., Milosavljević, D.D., Pantić, L.S.: A review of concentrating solar power plants in the world and their potential use in Serbia. Renew. Sustain. Energy Rev. **16**(6), 3891–3902 (2012). https://doi.org/10.1016/j.rser.2012.03.042
40. De Laquil, P., III, Kearney, D., Geyer, M., Diver, R.: Solar-thermal electric technology. Island Press, Washington, DC (United States), United States (1993)
41. Chemisana, D.: Building integrated concentrating photovoltaics: a review. Renew. Sustain. Energy Rev. **15**(1), 603–611 (2011). https://doi.org/10.1016/j.rser.2010.07.017
42. Aiuchi, K., Yoshida, K., Katayama, Y., Nakamura, M., Nakamura, K.: Sun tracking photosensor for solar thermal concentrating system
43. Rabl, A.: Active Solar Collectors and Their Applications, vol. 1. Oxford University Press, New York (1985)
44. Ibrahim, S.M.J.R.E.: The forced circulation performance of a sun tracking parabolic concentrator collector. **9**(1–4), 568–571 (1996)
45. Brunotte, M., Goetzberger, A., Blieske, U.: Two-stage concentrator permitting concentration factors up to 300x with one-axis tracking. Sol. Energy **56**(3), 285–300 (1996). https://doi.org/10.1016/0038-092X(95)00107-3
46. Grass, C., Schoelkopf, W., Staudacher, L., Hacker, Z.: Comparison of the optics of non-tracking and novel types of tracking solar thermal collectors for process heat applications up to 300 °C. Sol. Energy **76**(1), 207–215 (2004). https://doi.org/10.1016/j.solener.2003.07.031
47. Sun, J., Wang, R., Hong, H., Liu, Q.: An optimized tracking strategy for small-scale double-axis parabolic trough collector. Appl. Therm. Eng. 1408–1420 (2017). https://doi.org/10.1016/j.applthermaleng.2016.10.187
48. Ullah, F., Min, K.: Performance evaluation of dual-axis tracking system of parabolic trough solar collector. In: IOP Conference Series: Materials Science and Engineering 2018, vol. 1, p. 012166. IOP Publishing
49. Badescu, V.: Different tracking error distributions and their effects on the long-term performances of parabolic dish solar power systems. Int. J. Solar Energy **14**(4), 203–216 (1994). https://doi.org/10.1080/01425919408909811
50. Jamil, U., Ali, W.: Performance tests and efficiency analysis of solar invictus 53S—a parabolic dish solar collector for direct steam generation. In: AIP Conference Proceedings 2016, vol. 1, p. 070018. AIP Publishing LLC
51. Yan, J., Cheng, Z.-R., Peng, Y.-D.: Effect of tracking error of double-axis tracking device on the optical performance of solar dish concentrator. Int. J. Photoenergy **2018**, 9046127 (2018). https://doi.org/10.1155/2018/9046127

52. Natarajan, S.K., Thampi, V., Shaw, R., Kumar, V.S., Nandu, R., Jayan, V., Rajagopalan, N., Kandasamy, R.K.J.I.J.O.E.R.: Experimental analysis of a two-axis tracking system for solar parabolic dish collector. **43**(2), 1012–1018 (2019)
53. Tibúrcio, B.D., Liang, D., Almeida, J., Garcia, D., Vistas, C.R.: Dual-rod pumping approach for tracking error compensation in solar-pumped lasers. J. Photonics Energy **9**(02) (2019). https://doi.org/10.1117/1.Jpe.9.028001
54. Tibúrcio, B.D., Liang, D., Almeida, J., Garcia, D., Vistas, C.R., Morais, P.J.: Highly efficient side-pumped solar laser with enhanced tracking-error compensation capacity. Opt. Commun. **460**, 125156 (2020). https://doi.org/10.1016/j.optcom.2019.125156
55. Tibúrcio, B.D., Liang, D., Almeida, J., Garcia, D., Catela, M., Costa, H., Vistas, C.R.: Tracking error compensation capacity measurement of a dual-rod side-pumping solar laser. Renew. Energy **195**, 1253–1261 (2022). https://doi.org/10.1016/j.renene.2022.06.114
56. Xie, W.T., Dai, Y.J., Wang, R.Z., Sumathy, K.: Concentrated solar energy applications using Fresnel lenses: a review. Renew. Sustain. Energy Rev. **15**(6), 2588–2606 (2011). https://doi.org/10.1016/j.rser.2011.03.031
57. Al-Jumaily, K.E.J., Al-Kaysi, M.K.A.: The study of the performance and efficiency of flat linear Fresnel lens collector with sun tracking system in Iraq. Renew. Energy **14**(1), 41–48 (1998). https://doi.org/10.1016/S0960-1481(98)00045-7
58. James, L.W., Williams, J.K.: Fresnel optics for solar concentration on photovoltaic cells. In, 1978/01/1, pp. 673–679. (1978)
59. Hiramatsu, M., Miyazaki, Y., Egami, T., Akisawa, A., Mizuta, Y.: Development of non-imaging Fresnel lens and sun-tracking device. In: 3rd World Conference on Photovoltaic Energy Conversion, 2003. Proceedings of, 11–18 May 2003, vol. 2383, pp. 2383–2385 (2003)
60. Whitfield, G.R., Bentley, R.W., Weatherby, C.K., Hunt, A.C., Mohring, H.D., Klotz, F.H., Keuber, P., Miñano, J.C., Alarte-Garvi, E.: The development and testing of small concentrating PV systems. Sol. Energy **67**(1), 23–34 (1999). https://doi.org/10.1016/S0038-092X(00)00045-1
61. Huang, F., Li, L., Huang, W.: Optical performance of an azimuth tracking linear Fresnel solar concentrator. Sol. Energy **108**, 1–12 (2014). https://doi.org/10.1016/j.solener.2014.06.028
62. Wang, H., Huang, J., Song, M., Hu, Y., Wang, Y., Lu, Z.: Simulation and Experimental study on the optical performance of a fixed-focus fresnel lens solar concentrator using polar-axis tracking. Energies **11**(4) (2018). https://doi.org/10.3390/en11040887
63. Yabe, T., Ohkubo, T., Uchida, S., Yoshida, K., Nakatsuka, M., Funatsu, T., Mabuti, A., Oyama, A., Nakagawa, K., Oishi, T., Daito, K., Behgol, B., Nakayama, Y., Yoshida, M., Motokoshi, S., Sato, Y., Baasandash, C.: High-efficiency and economical solar-energy-pumped laser with Fresnel lens and chromium codoped laser medium.**90**(26), 261120 (2007). https://doi.org/10.1063/1.2753119
64. Yabe, T., Uchida, S., Ikuta, K., Yoshida, K., Baasandash, C., Mohamed, M.S., Sakurai, Y., Ogata, Y., Tuji, M., Mori, Y., Satoh, Y., Ohkubo, T., Murahara, M., Ikesue, A., Nakatsuka, M., Saiki, T., Motokoshi, S., Yamanaka, C.: Demonstrated fossil-fuel-free energy cycle using magnesium and laser. Appl. Phys. Lett. **89**(26), 261107 (2006). https://doi.org/10.1063/1.2423320
65. Perini, S., Tonnellier, X., King, P., Sansom, C.J.S.E.: Theoretical and experimental analysis of an innovative dual-axis tracking linear Fresnel lenses concentrated solar thermal collector **153**, 679–690 (2017)
66. Vasylyev, V.P., Tovmachenko, O.G., Vasylyev, S.V.: Expected optical performances of novel type multi-element high-heat solar concentrators. In: Proceedings ASES Conference (2002)
67. Tiburcio, B.D., Liang, D., Almeida, J., Matos, R., Vistas, C.R.: Improving solar-pumped laser efficiency by a ring-array concentrator. J. Photonics For. Energy **8**(1) (2018). https://doi.org/10.1117/1.Jpe.8.018002
68. Matos, R., Liang, D., Almeida, J., Tibúrcio, B.D., Vistas, C.R.: High-efficiency solar laser pumping by a modified ring-array concentrator. Opt. Commun. **420**, 6–13 (2018). https://doi.org/10.1016/j.optcom.2018.03.027

69. Garcia, D., Liang, D., Tibúrcio, B.D., Almeida, J., Vistas, C.R.: A three-dimensional ring-array concentrator solar furnace. Sol. Energy **193**, 915–928 (2019). https://doi.org/10.1016/j.solener.2019.10.016
70. Tibúrcio, B.D., Liang, D., Almeida, J., Garcia, D., Catela, M., Costa, H., Vistas, C.R.: Improving side-pumped solar lasers using ring-array concentrators. Int. J. Sustain. Energy 1–21 (2021). https://doi.org/10.1080/14786451.2021.1987435
71. Liang, D., Almeida, J., Vistas, C.R., Guillot, E.: Solar-pumped Nd:YAG laser with 31.5 W/m^2 multimode and 7.9 W/m^2 TEM$_{00}$-mode collection efficiencies. Solar Energy Mater. Solar Cells **159**, 435–439 (2017). https://doi.org/10.1016/j.solmat.2016.09.048
72. Geraldes, J.P., Liang, D.: An alternative solar pumping approach by a light guide assembly elliptical-cylindrical cavity. Sol. Energy Mater. Sol. Cells **92**(8), 836–843 (2008). https://doi.org/10.1016/j.solmat.2008.01.019
73. Mehellou, S., Liang, D., Almeida, J., Bouadjemine, R., Vistas, C.R., Guillot, E., Rehouma, F.: Stable solar-pumped TEM$_{00}$-mode 1064 nm laser emission by a monolithic fused silica twisted light guide. Sol. Energy **155**, 1059–1071 (2017). https://doi.org/10.1016/j.solener.2017.07.048
74. Bouadjemine, R., Liang, D., Almeida, J., Mehellou, S., Vistas, C.R., Kellou, A., Guillot, E.: Stable TEM00-mode Nd:YAG solar laser operation by a twisted fused silica light-guide. Opt. Laser Technol. **97**, 1–11 (2017). https://doi.org/10.1016/j.optlastec.2017.06.003